RSC Advances

PAPER

View Article Online
View Journal | View Issue

Cite this: *RSC Adv.*, 2017, **7**, 43172

Fabrication of N-doped and shape-controlled porous monolithic carbons from polyacrylonitrile for supercapacitors†

Yu Shu,[a] Jun Maruyama,[b] Satoshi Iwasaki,[b] Shohei Maruyama,[b] Yehua Shen[c] and Hiroshi Uyama*[ac]

Received 23rd June 2017
Accepted 28th August 2017

DOI: 10.1039/c7ra07003a

rsc.li/rsc-advances

N-doped porous monolithic carbons (PMC) have been developed from polyacrylonitrile (PAN) *via* a template-free thermally induced phase separation (TIPS) approach followed by an easy pyrolysis process. Three-dimensional (3D) PAN monolith (PM) was firstly fabricated as the starting material. The shape of the 3D PM was designed during the phase separation step, revealing that the product carbons had the potential advantages of desired porosity and controllable shape. Two typical activation methods were employed and compared to prepare PMC. KOH-activated PMC showed a larger surface area of 1600 $m^2\ g^{-1}$ and higher nitrogen content of 5.6% in comparison to that being activated in a carbon dioxide atmosphere (CD-PMC). The electrochemical measurements revealed that PMC possessed a high capacitance of 270 F g^{-1} at 0.2 A g^{-1} and 195 F g^{-1} even at 100 A g^{-1}, ultra-high rate capability with 72% capacitance retention from 0.2 to 100 A g^{-1} and outstanding cycling stability with 100% capacitance retention at 20 A g^{-1} after 5000 cycles. These results demonstrate that the present facile and efficient synthetic strategy for PMC from PAN can benefit the promotion of its application in energy storage devices and it is highly likely to be extended to other polymer sources.

1. Introduction

Supercapacitors (SCs), also called electrochemical capacitors, have drawn great attention in satisfying the increasing demands of portable electronic, energy storage systems and various electric vehicles because of their high power density, rapid charge/discharge capability and long cyclic life.[1–4] In principle, they can be broadly classified into two categories based on the distinct charge-storage mechanisms: one is the electric double-layer capacitors (EDLCs), in which the capacitance comes from plentiful charges accumulated at the electrode/electrolyte interface; another is the pseudo-capacitors, in which the capacity is related to the faradaic redox reactions on the surface of electrode.[5–7] Thus, the performance of SCs strongly depends on the physical and chemical properties of the adopted electrodes. Carbon-based materials are considered to be promising electrode candidates for SCs owing to their high surface area, controllable porous distribution, and suitable conductivity.[8–10] The precursors for carbon materials are various, including inorganic, organic, and complex compounds. Desired electric properties have been achieved by using the electrodes from graphene,[11–13] carbon nanotube,[14,15] and ordered mesoporous carbon,[16] but the costs were tremendous or the preparation procedures were complicated. Therefore, the synthesis of low-cost carbon materials with excellent electrochemical properties by a facile approach is of great significance in developing outstanding energy storage systems.

Recently, the modifications of surface functionalities with heteroatoms, such as N, O, B, S, or P, have been discovered effectively to adjust the electron donor/acceptor properties of carbon materials giving rise to additional pseudo-capacitance and maintain the excellent rate capability and cycling stability.[17–19] More and more heteroatom-doped carbon materials have been synthesized and N-doping is evidenced to be positive in improving the capacity by enhancing the electronic conductivity and surface wettability.[20–23] Traditional N-doped carbons are usually prepared by introducing a certain amount of N into carbon frameworks through a post-treatment process, such as treat with ammonia, urea, amines, *etc.*; however, it often results in a lower content of nitrogen.[24] Compared to the post-treatment process, pyrolysis directly of N-containing polymer precursors such as polypyrrole,[25] polyaniline,[26] and polyacrylonitrile (PAN)[27] seems to be more effective to get carbons

[a]*Department of Applied Chemistry, Graduate School of Engineering, Osaka University, Suita, Osaka 565-0871, Japan. E-mail: uyama@chem.eng.osaka-u.ac.jp*

[b]*Research Division of Environmental Technology, Osaka Research Institute of Industrial Science and Technology, 1-6-50 Morinomiya, Joto-ku, Osaka 536-8553, Japan*

[c]*Key Laboratory of Synthetic and Natural Functional Molecule Chemistry of Ministry of Education, College of Chemistry and Materials Science, Northwest University, Xi'an, Shaanxi Province, 710127, PR China*

† Electronic supplementary information (ESI) available: Supplementary figures. See DOI: 10.1039/c7ra07003a

with higher N content. Among the polymers mentioned above, PAN, a widely used precursor for synthesizing carbon materials, possesses a nitrogen atom per monomeric unit and forms an infusible stable ladder structure after a cyclization reaction to withstand the further high temperature. However, PAN was mainly employed to prepare carbon fibers.[28–33] Limited reports were related to activated carbons or monolithic carbons from PAN through an easy pyrolysis process. In our previous study, 3D monoliths with uniform meso/macro-porosity have been fabricated by a template-free thermally induced phase separation (TIPS) approach. The shapes of the monolith can be freely designed, which are advantageous for large-scale industrial applications.[34] Moreover, the derived activated carbons kept a microstructure even after heating at a high temperature and interestingly possessed high adsorption capacity for carbon dioxide.[35] Considering these merits of PAN and TIPS, it is highly promising to develop novel porous carbons with large surface area, nitrogen self-doped, and controllable shape to high performance SCs.

In this study, N-doped porous monolithic carbons (PMC) were obtained from PAN by the low-cost and facile template-free TIPS approach followed by a pyrolysis process. The fabricated PAN monolith (PM), as the precursor to prepare carbons, showed a three-dimensional (3D) porous structure. The shape of PM can be designed during the phase separation process, which will be beneficial to give the further product carbons a controllable shape. Subsequently, two typical pyrolysis methods including carbon dioxide and potassium hydroxide activation were employed and compared to obtain PMC with desired properties. The specific surface areas and porosity parameters were systematically investigated and the electrochemical performances were fully evaluated on both three- and two-electrode systems. In comparison with PMC prepared by carbon dioxide activation (CD-PMC), KOH-activated PMC possessed a large surface area, suitable pore size distribution, and high N content, resulting in a high specific capacitance, excellent cycle stability, and long cycle life. These results demonstrated that the PAN-based monolithic carbons presented herein are highly promising electrode candidate for energy storage devices.

2. Experimental

2.1. Fabrication of PAN monolith

Polyacrylonitrile copolymer (PAN) was obtained from Mitsubishi Rayon Co. Ltd. as the precursor. 3D porous PAN monolith (PM) was fabricated *via* a template-free TIPS approach as follows. PAN (0.42 g) was firstly dissolved in *N*,*N*-dimethylformamide/deionized water (DMF/H_2O, 85/15 wt%, 6 mL) solution. The mixture was stirred and heated at 85 °C until PAN was completely dissolved. Then, the clear solution was cooled at 25 °C overnight for the phase separation. The formed gel was immersed in methanol under mild shaking to remove DMF. Finally, 3D PM was obtained by drying under a reduced vacuum for one day. Meanwhile, monoliths with various shapes could be formed through the vessels used during the phase separation process.

2.2. Preparation of porous monolithic carbon

The PM was firstly subjected to oxidative stabilization by heating at 230 °C for 6 h under the presence of air. After naturally cooling to room temperature, the stabilized PM (SPM) was calcined at 600 °C for 1 h under the argon atmosphere to obtain the pre-carbonized SPM (PSPM). Subsequently, KOH activation was performed as follows: a given mass of PSPM was blended with KOH particles (PSPM/KOH mass ratio: 1/1), and the blend was heated at 200 °C, 500 °C, and finally at 800 °C for 1 h in each step in a furnace under the protection of N_2 flow. After cooling down to room temperature, the sample was washed sequentially with 1 M HCl and then deionized water until the pH became neutral. Finally, the sample was dried at 105 °C for 1 day, which was denoted as PMC. For comparison, SPM was carbonized and activated in a furnace under Ar/CO_2 (75/25 wt%) atmosphere at 950 °C for 1 h. The final product was taken out until the furnace cooled to a room temperature and donated as CD-PMC.

2.3. Characterization

The morphologies and microstructures were observed by a scanning electron microscopy instrument (SEM, HITACHI SU 3500). Thermogravimetric (TG) analysis was performed in a temperature range of 40–550 °C under N_2 atmosphere using a Seiko EXSTAR SII TG/DTA 7200 thermal analyzer. Fourier transform infrared radiation (FTIR) analysis was conducted by a Thermo Scientific Nicolet is5 in a wavenumber range of 4000–400 cm^{-1}. Nitrogen adsorption/desorption isotherms were plotted at 77 K by a Quantachrome NOVA 4200e Surface Analyzer. The specific surface area was calculated by Brunauer–Emmett–Teller (BET) method. Pore size distribution was determined by using the non-local density functional theory (DFT) and Horvath–Kawazoe (HK) models. The total pore volume was estimated from the adsorbed amount at a relative pressure around 0.99. Surface elemental composition was captured by energy dispersive X-ray spectroscopy (EDX, HITACHI, Miniscope TM 3000 equipped with Swift ED 3000) and elemental content was tested by a CHN Corder. X-ray diffraction (XRD) patterns were recorded in the 2θ range from 10 to 80° using a Rigaku SmartLab diffractometer with Cu Kα radiation sources. X-ray photoelectron spectroscopy (XPS) measurement was carried out on an AXIS-ULTRA DLD spectrometer (Kratos Analytical) with Al Kα X-ray radiation as X-ray source for excitation.

2.4. Electrochemical measurements

The electrochemical performances were investigated in both three- and two-electrode configurations by cyclic voltammetry (CV) and galvanostatic charge/discharge (GCD) measurements. All electrochemical tests were carried out in CHI7002E electrochemical instrument (BAS Inc. ALS 7002E) under ambient temperature.

Firstly, a three-electrode system was assembled by using 1 M H_2SO_4 as the aqueous electrolyte, platinum wire as the counter electrode, Ag/AgCl as the reference electrode, and glassy carbon (4 mm diameter) as the working electrode. The working

electrode was prepared as follows: 20.0 mg active samples (powder size < 45 μm) were mixed with 1 mL 0.8 wt% Nafion solution (diluted by isopropanol from 5% Nafion®) and sonicated for 30 min to form a well-dispersed ink, 3.5 μL of which was casted into the surface of the glassy carbon electrode. CV measurements were performed in a potential range of 0 V to 0.8 V *vs.* Ag/AgCl by varying scan rates from 1 to 500 mV s^{-1}. GCD measurements were carried out at current density at 0.2–100 A g^{-1}. The cycling life was evaluated by the GCD measurement at a constant current density of 20 A g^{-1} for 5000 and 10 000 cycles. The specific capacitance (C, F g^{-1}) obtained from CV was calculated by the following equation:

$$C = (q_a + q_c)/(2m\Delta V) \quad (1)$$

where q_a and q_c are the integrated anodic and cathodic voltammetric charges, respectively; m and ΔV refer to the mass of active material and the employed potential window.

The specific capacitance (C, F g^{-1}) calculated from the discharge process of the GCD curves was obtained by the equation:

$$C = I\Delta t/(m\Delta V) \quad (2)$$

where I is the current, Δt is the discharging time, and ΔV is voltage change excluding the IR drop during the discharge process.

Electrochemical impedance spectroscopy (EIS) was measured in the frequency range from 10^{-2} Hz to 10^{4} Hz at 0 V with voltage amplitude of 10 mV in 1 M H_2SO_4 electrolyte. The PMC-based working electrodes were prepared as follows. A homogenized slurry consisting of 85 wt% PMC (powder size < 45 μm), 10 wt% acetylene black, and 5 wt% polytetrafluoroethylene (PTFE) binder was rolled into a thin film. Then, the film was dried at 120 °C for one day and punched into a circular sheet (6 mm diameter). The PMC-based carbon sheet was pressed on the surface of SUS mesh as the working electrode. A platinum wire and an Ag/AgCl electrode were used as the counter electrode and the reference electrode, respectively.

The practical electrochemical performance was fully evaluated in a two-electrode system. Before the electrochemical tests, the PMC-based carbon sheet (6 mm diameter) and separator were sufficiently vacuum-impregnated with 1 M H_2SO_4 aqueous solution overnight. The two-electrode symmetrical system was assembled in a 2E-CELL-SUS cell (Eager Corporation, Japan) by using two nearly identical (weight and size) and fully impregnated carbon sheets as electrodes and polypropylene nonwoven cloth as a separator (Fig. S1†). The average weight of each electrode was around 2 mg. For comparison, commercial activated carbon (YP-50F, Kuraray Chemical Co.) was also tested in the same condition. The CV and GCD measurements were carried out in the potential window of 0–1.0 V. The specific capacitance of the total symmetrical SC cell (C_t, F g^{-1}) was obtained based on the GCD measurements from the equation:

$$C_t = I\Delta t/(2m\Delta V) \quad (3)$$

where I (A) is the charge/discharge current, Δt (s) is the discharging time excluding the IR drop, m (g) is the mass of active sample on the single electrode, and ΔV (V) is the voltage change excluding the IR drop during the discharge process.

The energy density (E_t, Wh kg^{-1}) and power density (P_t, W kg^{-1}) of the symmetric SC were calculated according to the following equations:

$$E_t = (C_t\Delta V^2)/(2 \times 3.6) \quad (4)$$

$$P_t = E_t/\Delta t \quad (5)$$

3. Results and discussion

3.1. Fabrication of monolith and its properties

PAN monolith (PM) was fabricated by TIPS approach and displayed a 3D porous structure. Several kinds of PM with various shapes were also prepared during the phase separation step and the 3D structure remained unchanged (Fig. S2†), revealing the feasible of the formation of shape-controlled product carbons. Thermal degradation behaviors of the raw PAN powder and it-derived PM were studied by the TG analysis (Fig. 1a). The dramatic weight loss of the used PAN powder and PM occurred from 320 to 460 °C, suggesting that the pyrolysis took place and volatile gases came out.[36] The resulting weight residues were about 49% at 500 °C for the prepared PM. Obviously, PM showed a higher total weight residue than that of the raw PAN powder, which may be due to the formation of internal 3D network and beneficial to get higher product yield after the further activation process. Nitrogen adsorption/desorption isotherms of PM followed typical type-IV isotherm with a large hysteresis loop at a high relative pressure, which means the presence of more or less disordered cylindrical or wedge-like pores (Fig. 1b). The obtained PM showed the BET surface area of 188 m^2 g^{-1} with the pore volume of 0.71 cm^3 g^{-1} and average pore size of 15 nm. The pore size distribution calculated by the non-local density functional theory (DFT) model exhibited a hierarchically porous structure including a few micropores, abundant mesopores and macropores (Fig. 1b, inset). The surface functional groups were analyzed by FTIR spectra (Fig. S3†). There was no clear difference between the raw PAN powder and the obtained PM. Furthermore, the surface elemental compositions were captured by EDX measurement

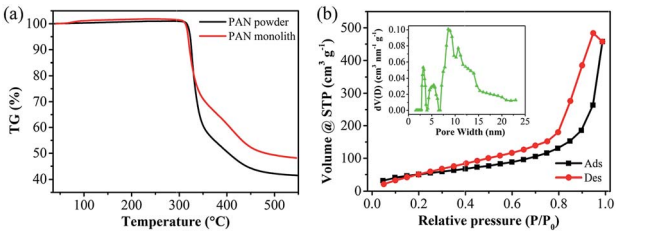

Fig. 1 TG curves of the used PAN powder and the fabricated PM (a), nitrogen adsorption/desorption isotherms with the inset of pore size distribution calculated by DFT model of PM (b).

(Table 1). The C, N, and O contents of PM were 67, 27, and 5.9 wt%, respectively. The prepared PM possessed the advantages of 3D hierarchical porous structure and enriched heteroatoms contents, endowing them with the great potential to further prepare porous carbons with large surface area, uniform pore distribution, and high nitrogen content.

3.2. Preparation and characterization of porous monolithic carbons

Two thermal treatment steps including stabilization (or pre-oxidation) and carbonization are necessary for the production of PAN-based carbons due to the property of pseudo-graphite microcrystal.[36] Stabilization process forms an infusible stable ladder structure which might be able to withstand a high temperature during the further pyrolysis process; and the carbonization process promotes to keep out non-carbon atoms and yield a turbostatic structure.[37] Thus, PM was firstly heated to get the stabilized PM (SPM). The primary reactions during this process, including oxidation, dehydrogenation, and cyclization, were speculated by FTIR spectra (Fig. S3†). The dramatic decrease in 2240 cm^{-1} (C≡N band) and obvious increase in 1587 cm^{-1} (C=N band) compared with that of PM, which can be interpreted by the 6-membered cyclization involving the formation of C=N.[36,38] The appearance of a small peak at 805 cm^{-1} corresponded to C=C–H stretching vibration revealed the dehydrogenation and subsequent isomerization of PM in this stabilization process.[39]

After the stabilization process, two methods were chosen to prepare porous monolithic carbons, one was that stabilized PM was directly activated under the existence of carbon dioxide to obtain CD-PMC; another was that SPM was first carbonized in the argon gas and then activated with an equal weight of KOH to get PMC. The micromorphology and microstructure of all samples were studied by SEM images (Fig. 2). No significant differences can be observed in the external shape of the four samples and the interconnected 3D porous structures still remained even after activation process.

The nitrogen adsorption/desorption isotherms and pore size distributions were illustrated to analyze the pore structure of PMC and CD-PMC. As shown in Fig. 3a, they both exhibited a type-I isotherm, while PMC possessed a higher adsorbed volume. The pore size was mostly smaller than 4 nm from DFT method and microporous size from the HK model was mainly

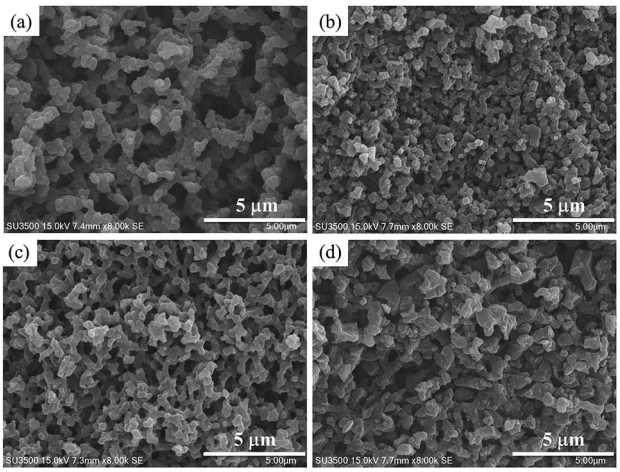

Fig. 2 SEM images of SPM (a), CD-PMC (b), PSPM (c), and PMC (d) under a same magnification.

distributed between 0.8 nm to 2 nm with a peak around 1.2 nm (Fig. 3b). The specific surface areas of PMC and CD-PMC measured by BET method were 1600 and 700 $m^2\ g^{-1}$, which were much higher than that of PM. The detailed summary of the specific surface area, pore volume, average pore size, and chemical composition of all samples was presented in Table 1. It can be seen that approximately 27 wt% of nitrogen was detected for PM and SPM from EDX spectrum, while 3.2% and 5.6% were obtained for CD-PMC and PMC from a CHN Corder. The nitrogen content decreased and carbon content increased after carbonization and activation process. Fig. 3c showed XRD patterns of CD-PMC and PMC. There were two characteristic peaks observed at around 24° and 43°, corresponding to the (002) and (10) diffractions, respectively. The XRD pattern of PMC showed weaker peak intensities than those of CD-PMC, corresponding to more disordered and smaller crystallites, which suggested the formation of the developed pore structure and relatively low graphitization degree.

XPS measurements were employed to analyze the components and chemical bondings at the surface of the carbon materials. The peaks of C 1s, N 1s, and O 1s were detected from the wide XPS survey spectrum. The high-resolution XPS spectra of C 1s, N 1s, and O 1s were collected to analyze the detailed information (Fig. 3d–f and S4†). The C 1s spectrum of PMC can

Table 1 BET surface area, total pore volume, average pore diameter, and chemical compositions of all samples

	From N_2 adsorption at 77 K			From EDX (wt%) or a CHN Corder (%)			
Sample	S_{BET}[a] ($m^2\ g^{-1}$)	V_{total}[b] ($cm^3\ g^{-1}$)	D_{ave}[c] (nm)	C (wt%)	N (wt%)	O (wt%)	H (%)
Raw PAN	—	—	—	67	28	5.2	—
PM	188	0.710	15.1	67	27	5.9	—
SPM	—	—	—	66	27	6.9	—
PSPM	8.95	0.017	7.57	71 (71%)	26 (19%)	3.5	2.1
CD-PMC	722	0.493	2.73	86 (72%)	7.8 (3.2%)	5.3	1.7
PMC	1600	0.862	2.16	83 (80%)	10 (5.6%)	6.0	0.5

[a] S_{BET} calculated by BET method. [b] Total pore volume (V_{total}) calculated at $P/P_0 \approx 0.99$. [c] Average pore diameter (D_{ave}).

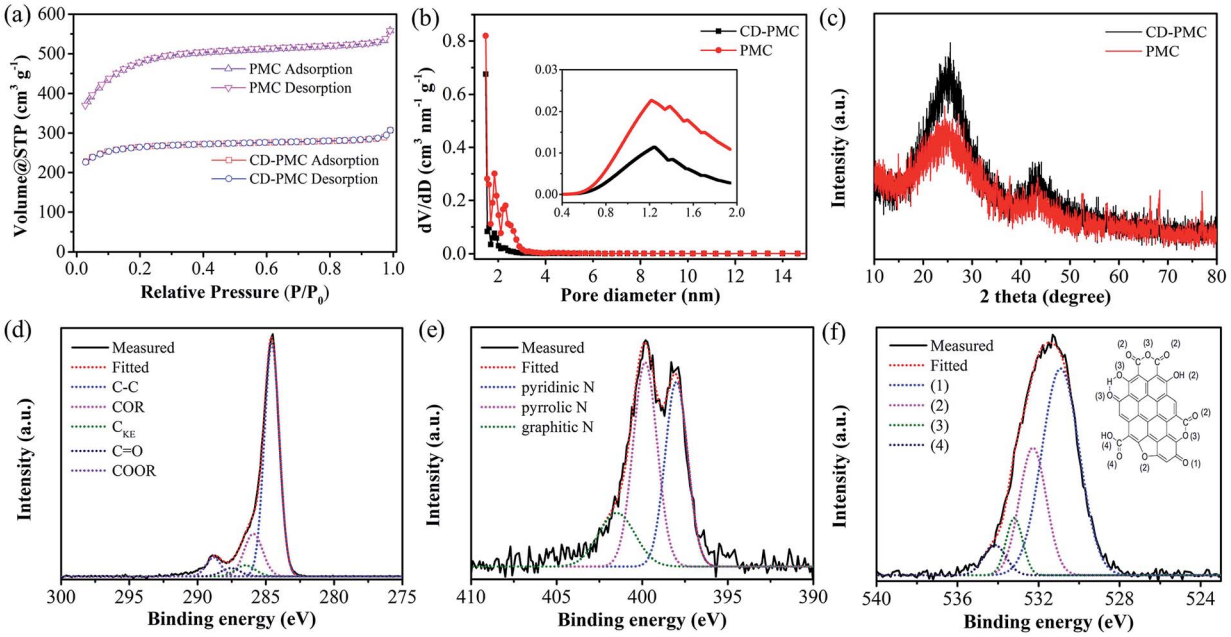

Fig. 3 N_2 adsorption/desorption isotherms (a) and pore size distributions calculated by DFT method with an inset of that by HK method (b) of CD-PMC and PMC, XRD patterns of CD-PMC and PMC (c), high-resolution XPS spectra and fitted data of C 1s peak (d), N 1s peak (e), and O 1s peak (f) for PMC.

be deconvoluted into five peaks located at 284.6, 285.9, 286.5, 287.6, and 288.8 eV (Fig. 3d), corresponding to aromatic and aliphatic carbon (C–C), hydroxyl and phenol groups (COR), carbon in keto–enol equilibria (C_{KE}), keto and quinone groups (C═O), and carboxylic groups (COOR), respectively. In the region of the N 1s core-level spectrum (Fig. 3e), the chemical states of the N atom, with binding energies of 398.3, 399.9 and 401.6 eV, can be identified as the pyridinic-N (N-6, ~34%), the pyrrolic-N (N-5, ~49%), and graphitic-N (N-G, ~17%), respectively.[40,41] Among them, N-5 and N-6 contribute to the pseudo-capacitance, while N-G promotes electron transport and effectively enhances the conductivity of carbon materials. Four characteristic peaks in the O 1s spectrum were centered at 531.5 eV, 532.4 eV, 533.3 eV, and 534.2 eV (Fig. 3f).[42,43] These peaks were assigned to C═O groups (group 1), carbonyl oxygen atoms in esters, amides, anhydrides and carbonyl oxygen atoms in hydroxyls or ethers (group 2), the ether oxygen atoms in esters and anhydrides (group 3), and the oxygen atoms in carboxyl groups (group 4). The atomic contents of C, N and O species of PMC were calculated quantitatively as 86, 2.6, and 11 at%, respectively. The high-resolution XPS spectra of the carbonized composite sample (CD-PMC) were also plotted in Fig. S4.† The C, N and O species were calculated quantitatively as 90, 2.8, and 7.0 at%, respectively. As shown in Fig. S4b,† three types of N-functionality were N-6 (~50%), N-5 (~39%), and N-G (~11%). The synergy of N-6, N-5 and N-G would contribute to the capacitance behavior greatly with pseudo-capacitance.

3.3. Electrochemical measurements

The electrochemical properties of PAN-based electrodes were accurately investigated by CV and GCD measurements in both three- and two-electrode systems. The electrochemical capacity was initially tested in the potential window of 0–0.8 V under the three-electrode system and the curves were plotted in Fig. 4 and 5. Generally, an ideal electrochemically active electrode material shows a nearly rectangular CV shape.[44] As shown in Fig. 4a, CD-PMC and PMC both displayed a quasi-rectangular CV shape at the scan rate of 5 mV s^{-1}, whereas PMC presented a larger integrated CV area, suggesting a higher specific capacitance.[45] The CV curves of PMC tested at different scan rates were displayed in Fig. 4b. The CV curves remained a satisfactory rectangular shape up to 200 mV s^{-1} indicating a typical electric double-layer capacitive behavior, and that the PMC-based electrode was stable in 1 M H_2SO_4 aqueous electrolyte. Even at 500 mV s^{-1}, an approximately rectangular shape was maintained, demonstrating a highly reversible adsorption/desorption of the electrolyte ions on the surface of the PMC electrode and an excellent rate performance. It must be mentioned that the occurred small humps in the range of 0.7 V to 0.8 V represented a character of faradaic pseudo-capacitance due to the redox reactions of N and O functional groups on the surface of PAN-based carbons.[27,46] Rate capability is considered as one key factor for the practical application of carbon-based electrodes. Fig. 4c showed the specific capacitances of CD-PMC and PMC as a function of scan rates. The specific capacitances were calculated by eqn (1) at various scan rates ranging from 1 to 100 mV s^{-1}. It is well known that the specific capacitance decreases with an increase of scan rate, which is attributed to the ion diffusion limitation among the highly porous structure channels.[47] As shown in Fig. 4c, PMC exhibited a much higher specific capacitance than that of CD-PMC, which may be due to its high specific surface area and suitable porous

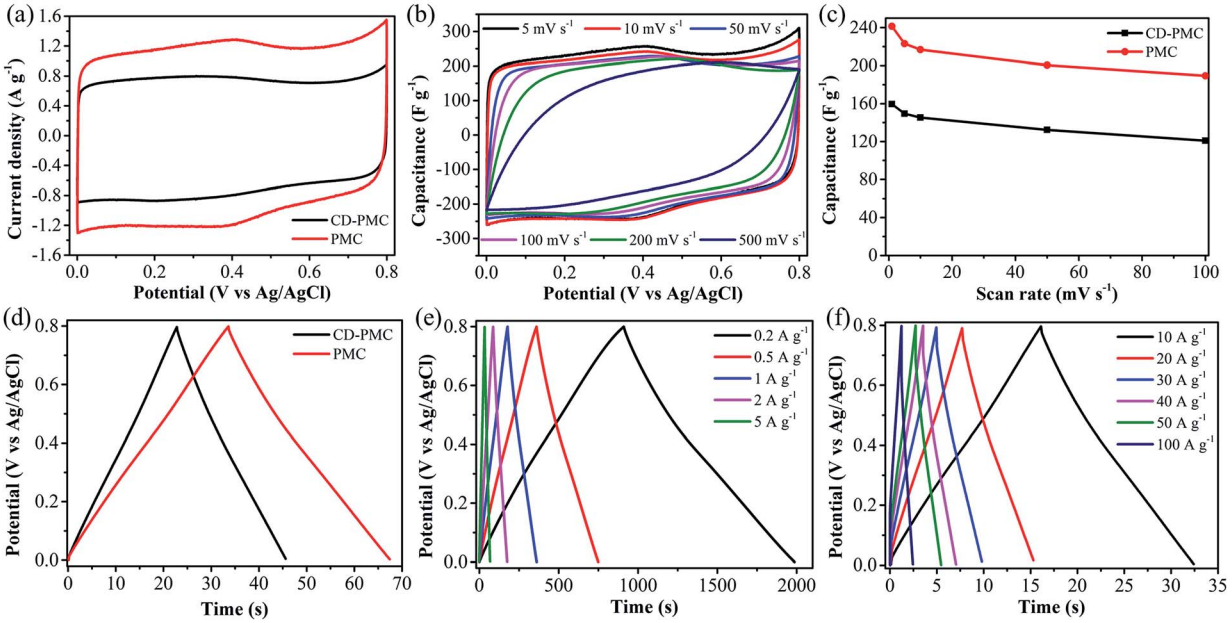

Fig. 4 CV curves of CD-PMC and PMC at a scan rate of 5 mV s^{-1} (a), CV curves of PMC at scan rates varying from 5 to 500 mV s^{-1} (b), comparison of specific capacitance as a function of scan rate for CD-PMC and PMC (c), GCD curves of CD-PMC and PMC at a current density of 5 A g^{-1} (d), GCD curves of PMC at current densities from 0.2 to 5 A g^{-1} (e) and 10 to 100 A g^{-1} (f).

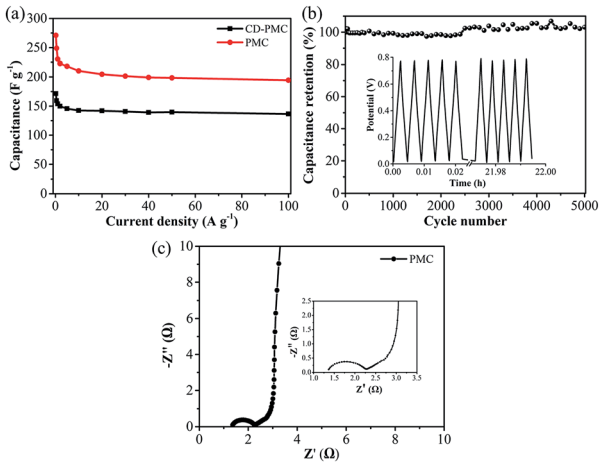

Fig. 5 Comparison of specific capacitance as a function of current density for CD-PMC and PMC (a), capacitance retention of PMC from GCD curves at a constant current density of 20 A g^{-1} for 5000 cycles with the first 5 and last 5 cycles inset (b), Nyquist plot of the PMC with the inset of enlarged high frequency region (c).

structures.[48] Furthermore, the capacitance retention of PMC displayed as high as 78% at a scan rate of 100 mV s^{-1} from 1 mV s^{-1}, representing a quick ion transport capability and excellent rate performance.

The GCD curves of CD-PMC and PMC measured in 1 M H_2SO_4 at a current density of 5 A g^{-1} were depicted in Fig. 4d. They both displayed a triangular shape which presented reversibility, an ideal electric double layer capacitive characteristic and high charge/discharge efficiency.[49] Theoretically, the longer charge/discharge time is, the more electrolyte ions would participate in the charge/discharge process, resulting in a higher specific capacitance.[50] In comparison with CD-PMC, PMC revealed a longer charge/discharge time and thus a higher specific capacitance. The GCD curves of PMC retained linearity and symmetry very well at current densities varying from 0.2 to 5 A g^{-1} (Fig. 4e). The typical isosceles triangular shape without obvious voltage drop represented an indication of excellent capacitive behavior of PMC. Even at high current densities ranging from 10 to 100 A g^{-1}, the triangular shapes were maintained and a small voltage drop occurred (Fig. 4f). The charge/discharge time significantly decreased with an increase of current densities because the electrolyte ions had sufficient time to enter and diffuse into the pores at low current densities.[51]

The gravimetric specific capacitances at various current densities ranging from 0.2 to 100 A g^{-1} were calculated by eqn (2) and plotted in Fig. 5a. The specific capacitances of CD-PMC and PMC almost remained unchanged after 10 A g^{-1}, indicating their superior rate capability. Obviously, PMC displayed higher specific capacitances than CD-PMC within the all range of current densities. The specific capacitances of PMC were 270 F g^{-1} at 0.2 A g^{-1}, and 195 F g^{-1} even at a very high current density of 100 A g^{-1}, resulting in a high capacitance retention rate of 72%. Cycling stability is another crucial factor in practical applications of the SCs. Therefore, the cycle life of PMC-based electrode was measured by GCD tests for 5000 charge/discharge cycles at a current density of 20 A g^{-1} within the potential window of 0–0.8 V (Fig. 5b). Remarkably, PMC possessed the outstanding cycle durability with the high retention rate of nearly 100% after 5000 cycles. The gradually increased capacitance between 2500 to 5000 cycles could be possibly attributed to the improved wettability and activing

process of this electrode, that is, the continuous diffusion of the electrolyte ions into the porosity would lead to the gradual increase in the effective charge storage sites of PMC-based electrode and thus the specific capacitance.[52] The GCD curves of the first and last five cycles were almost identical isosceles triangles, demonstrating an excellent long-term cycle stability of PMC (Fig. 5b, inset). Furthermore, there was almost no capacitance decay after 10 000 cycles for PMC-based electrode (Fig. S5†). And the GCD curves of the 5000th cycle and 10000th cycle remained unchanged. EIS measurements were performed at room temperature in the 1 M H_2SO_4 electrolyte to explore the frequency response characteristics of PMC (Fig. 5c). The Nyquist plots of PMC-based electrode displayed a small semicircle and nearly vertical line, indicative of a low contact resistance and good capacitive response.

In order to further investigate the electrochemical capacitive practical performances for the PAN-based carbon electrodes, a symmetric SC was assembled with two nearly identical (weight and size) carbon films as the electrodes and 1 M H_2SO_4 aqueous solution as the electrolyte. For comparison, the commercial activated carbon (YP-50F) was also tested. Fig. 6a showed that the CV curves of the three kinds of electrodes were tested at scan rate of 5 mV s^{-1} under the potential window of 0–1 V. It was clearly observed that all CV curves exhibited a relatively rectangular shape and PMC-based SC possessed the largest integrated CV area, which was consistent with the above results of that tested in the three-electrode system. In this as-assembled practical SC, carbon-based electrodes were sufficiently impregnated in the aqueous electrolyte solution and then directly used without the addition of electrolyte (Fig. S1†). Therefore, the electrochemical performance of the SC was strongly determined by the capability of electrodes. The surface morphology of the carbon films were observed by SEM images (Fig. S6†). The electrodes from CD-PMC and PMC showed a similar surface appearance. In addition, the capacitive behaviors of electrodes were also dependent on the wettability of the inner pores for the electrolyte.[53] Contact angle (CA) measurement was also carried out to study the surface wettability of all electrodes for 1 M H_2SO_4 aqueous electrolyte, which was used to preliminary evaluate the performance of the electrodes for SCs (Fig. S6,† inset).[54] PMC-based electrode gave a smaller CA value, which was in agreement with the larger CV integrated area, and thus a higher specific capacitance. The CV curves of PMC-based SC remained a relatively rectangular shape at various scan rates from 5 to 500 mV s^{-1}, indicating a near-ideal capacitive behavior with good rate performance (Fig. 6b). The GCD curves of three kinds of electrodes at a constant current density of 0.5 A g^{-1} exhibited typical triangle shapes without obvious voltage drops, indicating excellent coulombic efficiency together with good double-layer capacitive performance (Fig. 6c). PMC-based SC showed the longest charge/discharge time, meaning the highest specific capacitance. The GCD curves of PMC at current densities ranging from 0.1 to 1 A g^{-1} were shown in Fig. 6d. All GCD curves exhibited good triangle-shapes and excellent coulomb efficient.

The relationships between the specific capacitance of the total symmetrical SC calculated by eqn (3) and the current densities were summarized in Fig. 7a. The specific capacitances of PMC-based SC were as high as 63 F g^{-1} at 0.1 A g^{-1}, and 40 F g^{-1} even at the high current density of 20 A g^{-1} (about 63% capacitance retention), which was obviously higher than the values of commercial AC-based SC. The energy density and power density of the PMC-based SC were calculated by eqn (4) and (5), respectively. And the Ragone plot was drawn in Fig. 7b. The energy density of the PMC-assembled SC decreased from 8.8 to 2.9 Wh kg^{-1} with increasing of current density from 0.1 to 20 A g^{-1}, while the power density reached to 3666 from 25 W kg^{-1}. PMC-based SC possessed higher energy/power densities than the

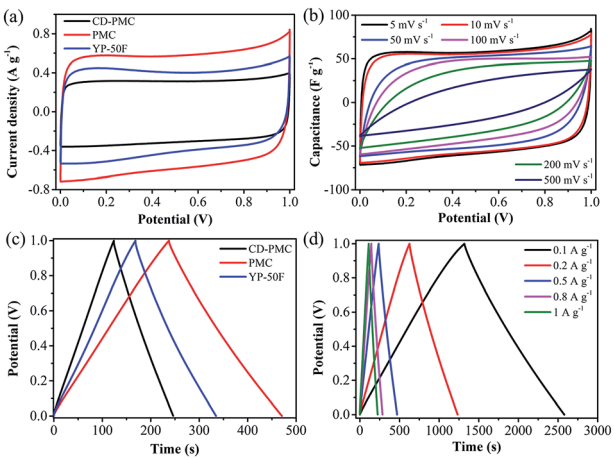

Fig. 6 Electrochemical performance tested in a two-electrode system with a potential window of 0–1 V. CV curves of CD-PMC, PMC, and YP-50F at a scan rate of 5 mV s^{-1} (a) and CV curves of PMC at scan rates from 5 to 500 mV s^{-1} (b), GCD curves of CD-PMC, PMC, and YP-50F at a current density of 0.5 A g^{-1} (c) and GCD curves of PMC at current densities from 0.1 to 1 A g^{-1} (d).

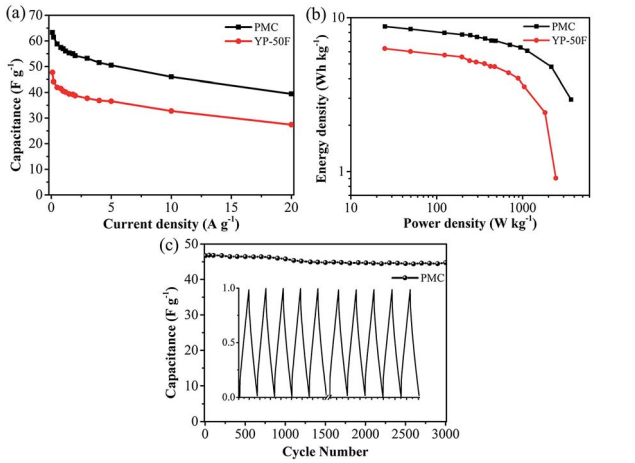

Fig. 7 The total specific capacitances of the symmetrical SCs from PMC and YP-50F as a function of current density (a), Ragone plot referring to the energy and power density of PMC and YP-50F-based SCs (b), capacitance retention of PMC-based SC from the GCD curves at a constant current density of 10 A g^{-1} for 3000 cycles with the first and last five cycles inset (c).

Table 2 Comparison of the electrochemical performance of PAN-based carbons for supercapacitors reported in the literature

Precursor	S_{BET} (m^2 g^{-1})	Electrolyte	Capacitance (F g^{-1})	Rate capacitance	Cycle stability	Cell[c]	Ref.
PAN	722	1 M H_2SO_4	108 at 0.05 A g^{-1}	50% from 0.05 to 20 A g^{-1}	—	3E	55
PAN/APEG	753	6 M KOH	302 at 0.2 A g^{-1}	56% from 0.2 to 40 A g^{-1}	95%	2E	56
PAN-b-PMMA	403	2 M KOH	314 at 0.5 A g^{-1}	68% from 0.5 to 20 A g^{-1}	90%	3E	57
			210 at 0.5 A g^{-1}	58% from 0.5 to 10 A g^{-1}	—	2E	
PAN	1165	6 M KOH	167 at 30 mV s^{-1}	67% from 0.75 to 6 A g^{-1}	78%	3E	58
PAN	3550	Organic[a]	216 at 0.05 A g^{-1}	56% from 0.05 to 10 A g^{-1}	100%	2E	59
PAN/CNT	613.8	1 M H_2SO_4	216 at 10 mV s^{-1}	63% from 10 to 200 mV s^{-1}	100%	3E	60
PAN/PANI	410	1 M H_2SO_4	335 at 0.5 A g^{-1}	52% from 0.5 to 32 A g^{-1}	—	3E	61
			—	—	86%	2E	
PAN	3130	Organic[b]	181 at 1 A g^{-1}	77% from 1 to 10 A g^{-1}	96%	2E	43
PMMA/PAN	2085	6 M KOH	314 at 0.5 A g^{-1}	83% from 1 to 20 A g^{-1}	96%	3E	27
PAN	1600	1 M H_2SO_4	270 at 0.2 A g^{-1}	72% from 0.2 to 100 A g^{-1}	100%	3E	This work
			253 at 0.1 A g^{-1}	62% from 0.1 to 20 A g^{-1}	96%	2E	

[a] 1 M $LiPF_6$ in EC/DMC: 1 M of $LiPF_6$ in a mixture of ethylene carbonate (EC) and dimethyl carbonate (DMC) (3 : 7 volume ratio). [b] $EMImBF_4$: ethyl-3-methylimidazolium tetrafluoroborate. [c] 3E: three-electrode system; 2E: two-electrode system.

commercial AC. Finally, the cycling performance of PMC-based SC was also evaluated using the GCD measurement and plotted in Fig. 7c. The specific capacitance displayed 47 F g^{-1} for the first cycle and remained at 45 F g^{-1} for the 3000th cycle with the retention of 96%, indicating that the charge/discharge process of PMC-assembled SC was highly reversible. The almost similar GCD curves of the first and the last five cycles revealed the good cycling and stability behaviors of the as-assembled SC (Fig. 7c, inset). Comparison with other reported carbons derived from PAN or its composites, as shown in Table 2, PMC herein demonstrated the desired specific capacitance, excellent rate capacitance and cycle stability not only in the three-electrode system but also in the symmetrical SC.

4. Conclusions

In this work, we developed a facile route for synthesis of N-doped and shape-controlled porous monolithic carbons from PAN *via* a template-free approach followed by an easy pyrolysis process and applied for the supercapacitors. Two typical activation methods were employed to prepare PMC with the advantages of large surface area, suitable pore size distribution, and high nitrogen content. Subsequently, the electrochemical performance was evaluated by CV and GCD measurements in both three- and two-electrode systems. PMC-based SC tested in a three-electrode system exhibited the high capacitance of 270 F g^{-1} at 0.2 A g^{-1} and 195 F g^{-1} at 100 A g^{-1}, the excellent capacitance retention of 72% from 0.2 to 100 A g^{-1}, the outstanding cycling stability with no capacitance decay at 20 A g^{-1} after 5000 cycles. In addition, the symmetric SC from PMC also displayed the high specific capacitance of 63 F g^{-1} at 0.1 A g^{-1} and superior cycle stability with the retention of 96% after 3000 cycles. The results demonstrated that the reported PMC herein is a highly promising electrode material for high performance supercapacitors. Furthermore, the facile and efficient route for N-doped and shape-controlled porous carbons can be readily extended to other types of nitrogen-containing polymer sources.

Conflicts of interest

There are no conflicts to declare.

Acknowledgements

This work was partly supported by the Hundred Talents Program, Shaanxi Province, PR China and a Grant-in-Aid for Scientific Research from the Japan Society for the Promotion of Science (No. 16K14081 and 17H03114). We also would like to thank Prof. Nobuhito Imanaka and Dr Shinji Tamura (Osaka University) for assistance with XRD measurement. Yu Shu thanks the China Scholarship Council (CSC) for a scholarship.

Notes and references

1 S. Chu and A. Majumdar, *Nature*, 2012, **488**, 294–303.
2 H. Jiang, P. S. Lee and C. Li, *Energy Environ. Sci.*, 2013, **6**, 41–53.
3 Q. Wang, J. Yan and Z. Fan, *Energy Environ. Sci.*, 2016, **9**, 729–762.
4 P. Simon and Y. Gogotsi, *Nat. Mater.*, 2008, **7**, 845–854.
5 P. Cheng, T. Li, H. Yu, L. Zhi, Z. Liu and Z. Lei, *J. Phys. Chem. C*, 2016, **120**, 2079–2086.
6 A. M. Bryan, L. M. Santino, Y. Lu, S. Acharya and J. M. C'Arcy, *Chem. Mater.*, 2016, **28**, 5989–5998.
7 L. Qie, W. Chen, H. Xu, X. Xiong, Y. Jiang, F. Zou, X. Hu, Y. Xin, Z. Zhang and Y. Huang, *Energy Environ. Sci.*, 2013, **6**, 2497–2504.
8 T. Sheng, Y. F. Xu, Y. X. Jiang, L. Huang, N. Tian, Z. Y. Zhou, I. Broadwell and S. G. Sun, *Acc. Chem. Res.*, 2016, **49**, 2569–2577.
9 S. Dutta, A. Bhaumik and K. C. W. Wu, *Energy Environ. Sci.*, 2014, **7**, 3574–3592.
10 T. Chen and L. Dai, *Mater. Today*, 2013, **16**, 272–280.
11 X. Yang, Y. S. He, G. Jiang, X. Z. Liao and Z. F. Ma, *Electrochem. Commun.*, 2011, **13**, 1166–1169.

12 J. Yan, Q. Wang, C. Lin, T. Wei and Z. Fan, *Adv. Energy Mater.*, 2014, **4**, 1400500.
13 D. Li, C. Yu, M. Wang, Y. Zhang and C. Pan, *RSC Adv.*, 2014, **4**, 55394–55399.
14 K. Shi, M. Ren and I. Zhitomirsky, *ACS Sustainable Chem. Eng.*, 2014, **2**, 1289–1298.
15 J. Patiño, N. López-Salas, M. C. Gutiérrez, D. Carriazo, M. L. Ferrer and F. D. Monte, *J. Mater. Chem. A*, 2016, **4**, 1251–1263.
16 G. Hasegawa, K. Kanamori, T. Kiyomura, H. Kurata, T. Abe and K. Nakanishi, *Chem. Mater.*, 2016, **28**, 3944–3950.
17 L. Zhou, H. Cao, S. Zhu, L. Hou and C. Yuan, *Green Chem.*, 2015, **17**, 2373–2382.
18 W. Deng, Y. Zhang, Y. Tan and M. Ma, *J. Electroanal. Chem.*, 2017, **787**, 103–109.
19 W. Deng, Y. Zhang, L. Yang, Y. Tan, M. Ma and Q. Xie, *RSC Adv.*, 2015, **5**, 13046–13051.
20 P. Chen, L. Wang, G. Wang, M. Gao, J. Ge, W. Yuan, Y. Shen, A. Xie and S. Yu, *Energy Environ. Sci.*, 2014, **7**, 4095–4103.
21 J. Li, K. Li, M. Li, D. Gosselink, Y. Zhang and P. Chen, *J. Power Sources*, 2014, **252**, 107–112.
22 Y. Deng, Y. Xie, K. Zou and X. Ji, *J. Mater. Chem. A*, 2016, **4**, 1144–1173.
23 Y. Tan, C. Xu, G. Chen, Z. Liu, M. Ma, Q. Xie, N. Zheng and S. Yao, *ACS Appl. Mater. Interfaces*, 2013, **5**, 2241–2248.
24 B. Cao, B. Zhang, X. Jiang, Y. Zhang and C. Pan, *J. Power Sources*, 2011, **196**, 7868–7873.
25 L. F. Chen, X. D. Zhang, H. W. Liang, M. Kong, Q. F. Guan, P. Chen, Z. Y. Wu and S. H. Yu, *ACS Nano*, 2012, **6**, 7092–7102.
26 X. Zhang, L. Ma, M. Gan, G. Fu, M. Jin, Y. Lei, P. Yang and M. Yan, *J. Power Sources*, 2017, **340**, 22–31.
27 L. Yao, G. Yang, P. Han, Z. Tang and J. Yang, *J. Power Sources*, 2016, **315**, 209–217.
28 Y. Lu, K. Fu, S. Zhang, Y. Li, C. Chen, J. Zhu, M. Yanilmaz, M. Dirican and X. Zhang, *J. Power Sources*, 2015, **273**, 502–510.
29 E. A. Morris, M. C. Weisenberger, M. G. Abdallah, F. Vautard, H. Grappe, S. Ozcan, F. L. Paulauskas, C. Eberle, D. Jackson, S. J. Mecham and A. K. Naskar, *Carbon*, 2016, **101**, 245–252.
30 S. Ma, J. Liu, Q. Liu, J. Liang, Y. Zhao and H. Fong, *Mater. Des.*, 2016, **95**, 387–397.
31 X. Wu, S. Mahalingam, A. Amir, H. Porwal, M. J. Reece, V. Naglieri, P. Colombo and M. Edirisinghe, *ACS Omega*, 2016, **1**, 202–211.
32 S. Perananthan, J. S. Bonso and J. P. Ferraris, *Carbon*, 2016, **106**, 20–27.
33 Y. Chen, Q. Liu and J. Wang, *J. Mater. Chem. A*, 2016, **4**, 5553–5560.
34 K. Okada, M. Nandi, J. Maruyama, T. Oka, T. Tsujimoto, K. Kondoh and H. Uyama, *Chem. Commun.*, 2011, **47**, 7422–7424.
35 M. Nandi, K. Okada, A. Dutta, A. Bhaumik, J. Maruyama, D. Derks and H. Uyama, *Chem. Commun.*, 2012, **48**, 10283–10285.
36 S. Lei, W. Cao, Z. Fu and L. Xu, *J. Appl. Polym. Sci.*, 2016, **133**, 43890.
37 M. S. A. Rahaman, A. F. Ismail and A. Mustafa, *Polym. Degrad. Stab.*, 2007, **92**, 1421–1432.
38 A. Palanisamy, N. V. Salim, B. L. Fox, P. Jyotishkumar, T. Pradeep and N. Hameed, *RSC Adv.*, 2016, **6**, 55792–55799.
39 L. Yao, G. Yang and P. Han, *RSC Adv.*, 2016, **6**, 43748–43754.
40 J. M. Jiménez Mateos and J. L. G. Fierro, *Surf. Interface Anal.*, 1996, **24**, 223–236.
41 J. Casanovas, J. M. Ricart, J. Rubio, F. Illas and J. M. Jiménez-Mateos, *J. Am. Chem. Soc.*, 1996, **118**, 8071–8076.
42 J. Maruyama, M. Umemura, M. Inaba, A. Tasaka and I. Abe, *J. Electrochem. Soc.*, 2009, **156**, A181–A186.
43 U. Zielke, K. J. Hüttinger and W. P. Hoffman, *Carbon*, 1996, **34**, 983–998.
44 Q. Wang, J. Yan, Y. Wang, T. Wei, M. Zhang, X. Jing and Z. Fan, *Carbon*, 2014, **67**, 119–127.
45 Y. Shu, A. Dobashi, C. Li, Y. Shen and H. Uyama, *Bull. Chem. Soc. Jpn.*, 2017, **90**, 44–51.
46 A. Choudhury, J. H. Kim, S. Sinha Mahapatra, K. S. Yang and D. J. Yang, *ACS Sustainable Chem. Eng.*, 2017, **5**, 2109–2118.
47 G. Zu, J. Shen, L. Zou, F. Wang, X. Wang, Y. Zhang and X. Yao, *Carbon*, 2016, **99**, 203–211.
48 X. Hao, J. Wang, B. Ding, Y. Wang, Z. Chang, H. Dou and X. Zhang, *J. Power Sources*, 2017, **352**, 34–41.
49 Q. Liang, L. Ye, Z. H. Huang, Q. Xu, Y. Bai, F. Kang and Q. H. Yang, *Nanoscale*, 2014, **6**, 13831–13837.
50 X. Gao, W. Xing, J. Zhou, G. Wang, S. Zhuo, Z. Liu, Q. Xue and Z. Yan, *Electrochim. Acta*, 2014, **133**, 459–466.
51 G. Ma, Q. Yang, K. Sun, H. Peng, F. Ran, X. Zhao and Z. Lei, *Bioresour. Technol.*, 2015, **197**, 137–142.
52 J. Zhou, J. Lian, L. Hou, J. Zhang, H. Gou, M. Xia, Y. Zhao, T. A. Strobel, L. Tao and F. Gao, *Nat. Commun.*, 2015, **6**, 8503.
53 D. G. Gromadskyi, J. H. Chae, S. A. Norman and G. Z. Chen, *Appl. Energy*, 2015, **159**, 39–50.
54 M. M. Vadiyar, S. C. Bhise, S. K. Patil, S. S. Kolekar, A. R. Shelke, N. G. Deshpande, J. Y. Chang, K. S. Ghule and A. V. Ghule, *Chem. Commun.*, 2016, **52**, 2557–2560.
55 H. Tenmyo, T. Asano, Y. Jo, K. Yoshii, T. Tsuda, J. Maruyama, H. Uyama and S. Kuwabata, *Electrochemistry*, 2015, **83**, 348–350.
56 K. Huang, M. Li, Z. Chen, Y. Yao and X. Yang, *Electrochim. Acta*, 2015, **158**, 306–313.
57 K. Yan, L. B. Kong, K. W. Shen, Y. H. Dai, M. Shi, B. Hu, Y. C. Luo and L. Kang, *Appl. Surf. Sci.*, 2016, **364**, 850–861.
58 Y. Xu, J. Sun, H. Chen and L. Bai, *RSC Adv.*, 2015, **5**, 37780–37788.
59 K. Gupta, T. Liu, R. Kavian, H. G. Chae, G. H. Ryu, Z. Lee, S. W. Lee and S. Kumar, *J. Mater. Chem. A*, 2016, **4**, 18294–18299.
60 Y. Wang, B. Fugetsu, Z. Wang, W. Gong, I. Sakata, S. Morimoto, Y. Hashimoto, M. Endo, M. Dresselhaus and M. Terrones, *Sci. Rep.*, 2017, **7**, 40259.
61 F. Miao, C. Shao, X. Li, K. Wang and Y. Liu, *J. Mater. Chem. A*, 2016, **4**, 4180–4187.

